Corrosion Resistance Enhancement of Type 420J2 Martensitic Stainless Steel by Laser Thermal Processing

Journal of The Electrochemical Society, 2026 **173** 101502

Corrosion Resistance Enhancement of Type 420J2 Martensitic Stainless Steel by Laser Thermal Processing

Tomoyo Manaka,[1,2,z] Yusuke Tsutsumi,[3,4] Mitsuhiro Goto,[5] Mariko Kadowaki,[3] Yoshiharu Murase,[3] Hideki Katayama,[3] Takuya Ishimoto,[1,2] and Takao Hanawa[6,7,8]

[1]*School of Sustainable Design, University of Toyama, Toyama 930-8555, Japan*
[2]*Titanium Research Center, University of Toyama, Toyama 930-8555, Japan*
[3]*Research Center for Structural Materials, National Institute for Materials Science, Tsukuba 305-0047, Japan*
[4]*School of Materials and Chemical Technology, Institute of Science Tokyo, Tokyo 152-8552, Japan*
[5]*Fuji Koushuha Industry Co., Ltd, Sakai 590-0001, Japan*
[6]*Graduate School of Medicine, Kobe University, Kobe 650-0047, Japan*
[7]*Institute of Science Tokyo, Tokyo 101-0062, Japan*
[8]*Graduate School of Engineering, Osaka University, Suita 565-0871, Japan*

A laser thermal processing method was developed to enhance the corrosion resistance of martensitic stainless steels, which typically offer high hardness but poor corrosion resistance. Specifically, type 420J2 martensitic stainless steel (420J2 SS) plates were subjected to laser irradiation, causing rapid heating and quenching that modified the microstructure. After processing, three distinct layers were observed from the surface downward: a remelted layer, a phase-transformed layer, and the substrate. The remelted layer was formed by localized melting from the laser heat, followed by rapid quenching and solidification. Corrosion-inducing inclusions within this layer melted into the matrix, and their reprecipitation was effectively suppressed. The microstructure of the remelted layer comprised fine needle-like features, along with martensitic and austenitic phases. Due to the dominance of the martensitic phase, the hardness of the remelted layer increased significantly. Consequently, the remelted surface exhibited improved corrosion resistance and hardness. In contrast, the microstructure and corrosion resistance of the inner layer remained similar to those of the untreated 420J2 SS, indicating that the laser thermal processing did not adversely affect the substrate. Overall, this method provides an effective means of improving both the corrosion resistance and surface hardness of martensitic stainless steels.
 [DOI: 10.1149/1945-7111/ae697d]

Manuscript submitted January 7, 2026; revised manuscript received April 15, 2026. Published May 18, 2026.

Stainless steels are widely used in applications ranging from structural components to medical devices. Their high corrosion resistance is largely attributed to the spontaneous formation of passive films on their surfaces, primarily composed of Cr oxide or Cr-hydrated oxyhydroxide.[1–3] However, despite this inherent resistance, stainless steels are susceptible to localized corrosion, such as pitting, particularly in Cl^- containing environments.[4]

Among various types of stainless steels—precipitation, hardening, ferritic, austenitic, and duplex—martensitic stainless steels exhibit the lowest corrosion resistance. This is partly due to their carbon content, which, while necessary for enhancing hardness through quenching, adversely affects corrosion resistance. Martensitic stainless steels are valued for their high hardness, strength, and wear resistance when subjected to appropriate heat treatments.[5] These properties make them suitable for medical tools such as surgical instruments that require sharp cutting edges. However, achieving both high hardness and good corrosion resistance is inherently challenging. As a result, the limited corrosion resistance of martensitic stainless steels restricts their applicability in environments that demand both mechanical performance and long-term corrosion durability.

Micron-scale sulfide inclusions, particularly manganese sulfide (MnS), are known to serve as initiation sites for corrosion in stainless steels.[6–12] Removing these inclusions from the surface can significantly enhance corrosion resistance. Additive manufacturing (AM) techniques, especially laser powder bed fusion (LPBF), are effective in reducing MnS content. LPBF involves melting and layering metal powders using a laser beam,[13] and studies have reported improved corrosion resistance in LPBF-fabricated 316 l and 420J2 stainless steels.[14–20] The rapid melting and solidification in LPBF suppress the reformation of inclusions, contributing to enhanced corrosion performance.[14,19,20] As schematically illustrated in Fig. 1, the suppression of inclusion reformation reduces the number of micro-galvanic sites, where anodic dissolution ($Fe \rightarrow Fe^{2+} + 2e^-$) occurs at locally active regions and cathodic oxygen reduction ($O_2 + 2H_2O + 4e^- \rightarrow 4OH^-$) proceeds on the surrounding surface, thereby improving corrosion resistance.

Despite its advantages, AM has limitations when applied to large-scale industrial manufacturing. High costs, long processing times, and restricted build volumes make it more suitable for high-value, small-sized components, such as those used in biomedical or aerospace applications. In contrast, general-purpose stainless-steel products, including structural materials, require scalable, cost-effective, and time-efficient processing methods. Moreover, LPBF cannot be applied post-manufacture to modify existing components.

To address these challenges, alternative techniques that can produce LPBF-like microstructures with reduced MnS content at lower cost and complexity are required. One promising approach involves laser-based surface treatments. Ultra-rapid cooling via laser irradiation can induce specific thermal histories in the surface layer, similar to those achieved by LPBF, without relying on powder-based processes. Laser surface modification of stainless steels has been studied previously.[21–24] For example, yttrium-aluminum-garnet laser treatments have been shown to form ferritic microstructures with homogenized chromium distribution or δ-ferrite, both of which improve pitting corrosion resistance.[21,22] However, the use of semiconductor lasers to selectively modify only the extreme surface layer of martensitic stainless steels, mimicking LPBF microstructures and corrosion resistance depending on irradiation conditions, has not been thoroughly explored. Furthermore, the impact of irradiation conditions on microstructural evolution and corrosion resistance, as well as the role of MnS inclusions, remains poorly understood.

In this study, we focused on laser thermal processing, a technique traditionally used for hardening and cladding, and adapted it to selectively melt a thin surface layer of martensitic stainless steel. We investigated whether this approach could generate LPBF-like surface microstructures with enhanced corrosion resistance. The effects of laser thermal processing on corrosion resistance, microstructural evolution, and hardness were systematically evaluated for both the treated surface layer and the underlying base material.

[z]E-mail: manaka@sus.u-toyama.ac.jp

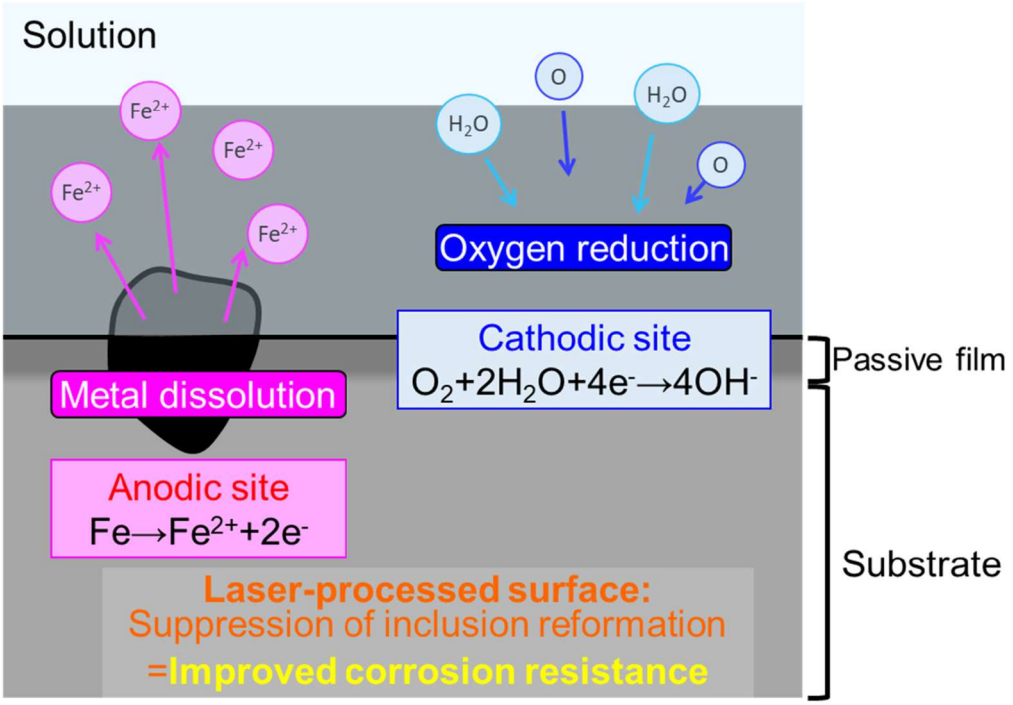

Figure 1. Schematic illustration of the corrosion mechanism on the laser-processed surface of Type 420J2 stainless steel in a neutral chloride solution, where anodic dissolution and cathodic oxygen reduction occur at locally separated sites, and suppression of inclusion reformation reduces micro-galvanic sites and improves corrosion resistance.

Experimental

Specimen preparation.—A martensitic 420J2 stainless steel (420J2 SS) plate (40 × 80 × 5 mm) (Test Materials Co., Ltd) was used in this study. The specimens were solution-treated and annealed according to the standard and had an HBW of 235 or less. Their chemical composition is presented in Table I. The surfaces of the specimens were mechanically wet ground using #150, #320, #600, and #800 waterproof abrasive SiC papers. Subsequently, the specimens were ultrasonicated twice in acetone and once in isopropanol for 600 s each.

The prepared 420J2 stainless steel specimens were subjected to laser thermal processing using the following procedure. Laser irradiation was performed using a semiconductor laser oscillator (LDF5000–100). The specimens were irradiated with a beam width of 10 mm at a scanning rate of 100 cm min^{-1} using laser powers of 950, 1100, 1650, 2000, 2500, 3000, 3500, or 4000 W. The irradiation was performed under atmospheric conditions in a large-sized enclosure, especially designed for processing large structures. The laser unit was positioned above the specimen, scanning from edge to edge along its longitudinal direction.

The width of the area exhibiting metallographic structural changes after one cycle of laser irradiation ranged from approximately 8.0 to 10.0 mm. For electrochemical measurements, both rims —including the interfaces between laser-irradiated and non-irradiated areas —were covered with insulating resin paint (SUNECON Mask Ace S, Taiyo Chemicals and Engineering Co., Ltd) to effectively evaluate the influence of laser irradiation on corrosion resistance. The resin adhered well to the specimen and prevented crevice corrosion by sealing gaps at the specimen–resin interface. Therefore, only the 7.5 mm wide laser-irradiated area was exposed to the test solution.

Table I. Chemical composition of 420J2 SS.

Element	Fe	Cr	Ni	C
Concentration (ppm)	Bal.	13.20	0.28	0.31
Element	P	S	Si	Mn
Concentration (ppm)	0.017	0.003	0.48	0.42

The thermally oxidized surface layer formed during laser processing was removed by mechanical polishing prior to subsequent analyses, including electrochemical measurements. The specimens were stored under controlled conditions at a constant temperature, and the elapsed time between laser processing and polishing was more than several days, while that between polishing and measurement was within several days.

Potentiodynamic polarization measurements.—Anodic polarization measurements were conducted to evaluate the effect of laser thermal processing on corrosion resistance. The specimen was placed in an electrochemical measurement cell, exposing only a circular measurement area to the solution. The original exposed area was 0.78 cm^2, but was reduced to 0.67 cm^2 due to the masking of the rims with an insulating resin paint, as described above. A Pt-coated Ti rod and an Ag/AgCl (3.33 M KCl) electrode were used as the counter and reference electrodes, respectively. A mixed aqueous solution of 0.1 M Na_2SO_4 and 0.585 M NaCl, simulating seawater chloride content, was used as the test solution at 297 ± 3 K.

Each electrode was connected to a potentiostat (HABF-501A, Meiden Hokuto Corp.), a function generator (HB-111, Meiden Hokuto Corp.), and a data logger (midi LOGGER GL220, Graphtec Corp.). The open-circuit potential (E_{corr}) was recorded after 600 s of immersion. A linearly increasing anodic potential scan at 20 mV min^{-1} was applied. Anodic polarization was initiated from E_{corr} − 100 mV to ensure stable initial conditions and reproducible measurements. Starting slightly below E_{corr} helps to minimize fluctuations near the open-circuit potential and enables a smooth transition to anodic polarization. The holding time at the initial potential was minimized to avoid surface modification such as cathodic alkalization. The test was stopped when the current density

reached 10 mA cm^{-2} after a rapid increase caused by pitting corrosion. The pitting potential (E_{pit}) was defined as the potential at which the current density reached 100 μA cm^{-2}. Each experiment was repeated five times under the same conditions to ensure reproducibility.

Surface and cross-sectional observation.—The surfaces and cross-sections of the specimens before and after laser thermal processing were observed using optical/laser microscopy (VK-X200, VHX-5000, Keyence Corp.) and scanning electron microscopy (SEM) equipped with an energy-dispersive X-ray spectroscopy (EDS) (TM4000Plus, Hitachi High-Tech Corp.). A cross-section approximately 2 mm from the specimen edge was analyzed after laser thermal processing.

The specimens were cut into small pieces and embedded in cold-mounting epoxy resin (Epofix, Struers LLC) to expose the cross-sectional surfaces. Each embedded specimen was mechanically ground using P150, P320, P600, and P800 grit abrasive SiC papers and then buff-polished to a mirror finish using 9 and 3 μm polycrystalline diamond and 1 μm Al_2O_3 suspension. For optical microscopy, the specimens were chemically etched to reveal metallographic structures using a solution of 33 ml of H_2O, 33 ml of ethanol, 33 ml of HCl, and 1.5 g of $CuCl_2$. The specimens were immersed in the etching solution at room temperature for 10 s and then rinsed with pure water. Before SEM/EDS analysis, the resin-embedded specimen surfaces were coated with Pt (Quick Auto Coater, SC-701AT, Sanyu Electron Co., Ltd).

Microstructural characterization.—Phase compositions were determined using X-ray diffraction (XRD; D8 ADVANCE, Bruker Corp.) and SEM (SU5000, Hitachi High-Tech Corp.) equipped with an electron backscatter diffraction (EBSD) detector (Digi View V EBSD camera, EDAX) to assess the effect of laser thermal processing on the crystal structure.

XRD data were acquired from the standard surface and from surfaces ground to depths of 50, 250, and 750 μm using a specimen processed at 2000 W. The surfaces were mechanically ground using P150, P320, P600, and P800 grit abrasive SiC papers, followed by buff-polishing with a 9 and 3 μm polycrystalline diamond, 1 μm Al_2O_3 suspension, and 0.06 μm colloidal silica suspension. The specimens were then ultrasonicated twice in acetone and once in isopropanol for 600 s each. Cu Kα radiation at 40 kV and 40 mA was used as the X-ray source, and data were collected over a 2θ range of 30–90°. Diffraction patterns were analyzed using PC software (DIFFRAC. EVA, Bruker Corp.).

EBSD data were acquired from the cross-sections of specimens processed at 950 and 2000 W, as well as unprocessed specimens. Surface preparation followed the same procedures as used for XRD specimens.

Vickers microhardness measurement.—Vickers hardness tests were performed to evaluate the effects of the laser thermal processing on the hardness of the material. The same specimens as those described in the *Microstructural characterization* section were employed. Hardness was measured using a Vickers microhardness tester (HMV-G 20S, SHIMADZU Corp.) with a 2.942 N load and a loading time of 15 s. Measurements were taken at 12 randomly selected points on each surface, and the average hardness was calculated from 10 values after excluding the maximum and minimum.

Results and Discussion

Material morphology.—The metallic luster of the laser-irradiated region disappeared after processing, and the surface appeared dull brown. This discoloration and roughened texture are attributed to thermally induced oxidation caused by high surface temperatures during laser thermal processing in atmospheric conditions.

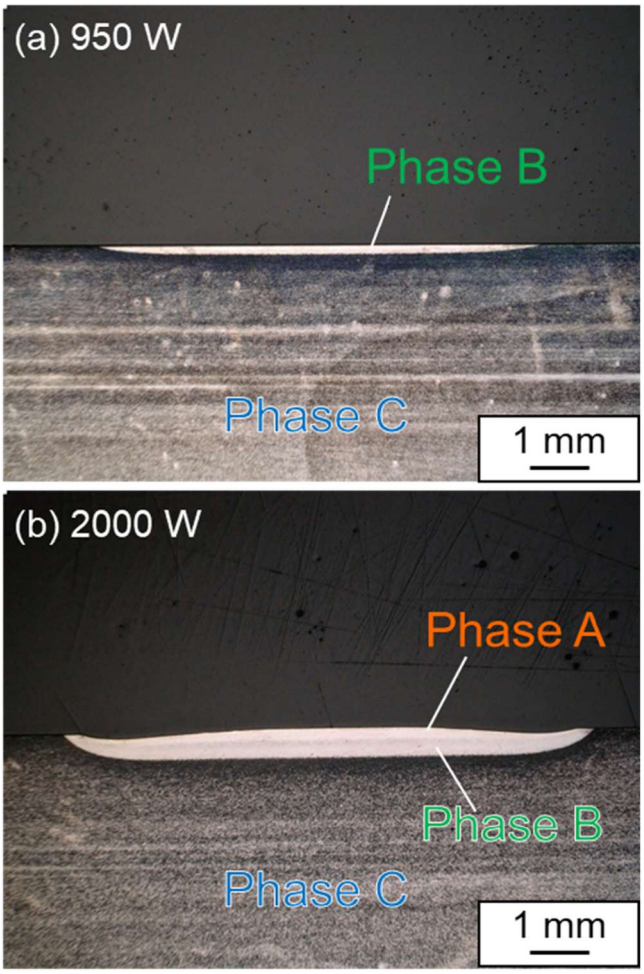

Figure 2. Optical micrographs of the cross-section of specimens subjected to laser thermal processing at (a) 950 and (b) 2000 W.

Cross-sectional images were acquired to examine how laser thermal processing altered the microstructure beneath the surface of the material. Specimens were etched to enhance the visibility of microstructural differences. Observations revealed distinct characteristics between specimens processed at 1100 W or lower and those processed at 1650 W or higher. Figure 2 shows optical micrographs of the specimens processed at 950 and 2000 W. The 950 W specimen exhibited a flat surface profile, whereas the 2000 W specimen displayed a slight central bulge along the laser irradiation line and shallow indentations on both sides. This morphology is attributed to the Gaussian-like energy distribution of the laser beam, which produces a higher power density at the center, resulting in preferential melting in this region. In addition, thermally induced surface tension gradients within the molten pool generate Marangoni convection, leading to the redistribution of molten material from the hotter central region toward the surrounding areas. As a result, material accumulates in the central region, forming a slight bulge, while shallow depressions are formed near the edges.[25,26] These observations indicate that the surface remains largely unmelted at 950 W, while pronounced surface melting and melt pool dynamics are evident at 2000 W. All micrographs revealed a bright-colored phase beneath the laser-irradiated area, contrasting with a darker underlying phase. The bright layer represents microstructural transformation under specific thermal conditions during laser irradiation. Specimens treated at 1650 W or higher exhibited two distinct bright layers in two phases termed "Phase A" (upper part) and "Phase B" (lower part). In contrast, only a single bright layer was observed in specimens processed at 950 and

Table II. Thicknesses of newly formed layers induced by laser thermal processing.

	Laser irradiation power (W)							
	950	1100	1650	2000	2500	3000	3500	4000
Phase A (μm)	—	—	110 −130	170 −210	220 −240	360	360	330
Phase B (μm)	180	270 −290	320 −370	440 −470	450 −480	490	460	340

1100 W, indicating the presence of only Phase B. Therefore, Phase A corresponds to the remelted region, while Phase B represents the phase-transformed zone without melting. To evaluate the spatial homogeneity of the Phase A layer, Vickers microhardness measurements were performed across the processed region. Although some scatter in hardness values was observed, no position-dependent trend was identified, suggesting that the microstructure within Phase A is nearly homogeneous. Phase depths increased with increasing irradiation power. The region beneath Phase B, which may have been moderately heated but not transformed, is hereafter referred to as "Phase C." Table II summarizes the irradiation powers and corresponding layer thicknesses of Phases A and B. With increasing laser power, the thickness of Phase A initially increases due to the higher energy input. However, at higher powers (⩾3000 W), the thickness of Phase A tends to saturate. This behavior is attributed to enhanced heat dissipation into the surrounding material and increased melt pool convection, which limit further deepening of the molten region. In contrast, Phase B is formed in regions experiencing sufficient heating without melting. At the highest power (4000 W), a larger volume of material exceeds the melting temperature, resulting in the expansion of Phase A and a corresponding reduction in the thickness of Phase B.

Microstructure.—Laser thermal processing-induced microstructural changes shown in Fig. 3 were analyzed using EBSD and XRD. Figure 3 displays the inverse pole figure (IPF) and phase maps of the unprocessed, 950 W-processed, and 2000 W-processed specimens. Martensitic phases typically exhibit a body-centered tetragonal (bct) structure.[27,28] However, because EBSD does not distinguish between ferrite (body-centered cubic, bcc) and martensite (bct) phases, both appear green in the phase maps.

The unprocessed 420J2 stainless steel microstructure (Figs. 3a and 3b) consisted of equiaxed ferrite grains with random orientation and small amounts of residual austenite. Figures 3c and 3d present the microstructure of the surface layer (Phase B) of the 950 W-processed specimen. This area corresponds to the bright layer in Fig. 1a. The microstructure consisted of acicular martensite and spherical austenite, some of which was surrounded by bcc phase, suggesting partial ferritic presence. The inner layer (Phase C, Figs. 3e and 3f) retained a microstructure (area corresponding to the dark layer in Fig. 1a) similar to the unprocessed specimen, indicating that no phase transformation occurred.

Figures 3g and 3h shows the microstructure of the top surface layer (Phase A) of the specimen processed at 2000 W. This area corresponds to the top of the bright layer in Fig. 1b. The top surface consists of acicular martensitic and relatively coarse austenitic microstructures. Figures 3i and 3j present the microstructure of the bottom surface layer (Phase B) of the 2000 W-processed specimen. This area corresponds to the bottom of the bright layer in Fig. 1b. The microstructure was similar to the top surface of the 950 W-processed specimen. Figures 3k and 3l show the microstructure of the inner layer (Phase C) of the 2000 W-processed specimen. This area corresponds to the dark layer in Fig. 1b. The microstructure is similar to the unprocessed specimen.

The XRD patterns of the 2000 W-processed specimen (Fig. 4) revealed peaks corresponding to bcc structures,[29,30] confirming ferrite as the primary phase. The Phase A layer displayed broader and weaker peaks, indicating reduced crystallinity. The full width at half maximum (FWHM) values decreased in the order: Phase A > Phase B > Phase C and the unprocessed, with peak intensity showing the opposite trend. The XRD peak shape and intensity of the Phase C layer were nearly identical to those of the unprocessed specimen. The large FWHM peaks indicate that the Phase A layer has a less crystalline microstructure than the original layer. Figure 4b shows the enlarged graph of the α (110) peak. An asymmetric α (110) peak was observed in Phase A, with peak splitting indicative of a bct structure,[31] confirming martensitic transformation. These findings align with the EBSD phase maps in Fig. 3. Laser thermal processing, therefore, enables the formation of engineered microstructural layers, several hundred micrometers deep, on specimen surfaces.

In addition, MnS inclusions, which are known to influence corrosion behavior, were observed in the unprocessed specimen, whereas they were not clearly detected in the remelted layer, as discussed in detail in Fig. 9.

Hardness.—Martensitic stainless steels are known to harden through heat treatments such as quenching.[32,33] Given the rapid cooling during laser thermal processing, significant surface hardening is expected. Further, the Phase A layer is composed of a martensitic structure owing to the rapid cooling conditions. Therefore, the hardness before and after laser thermal processing was investigated.

Figure 5 shows the Vickers microhardness profile of the 2000 W-processed specimen. The unprocessed specimen had a hardness of 175 HV, while that of Phase A exceeded 690 HV, confirming substantial hardening due to martensitic transformation. This result is consistent with the XRD diffraction pattern (Fig. 4) and the EBSD phase map (Fig. 3h), which confirms the presence of martensite in Phase A. Generally, the martensitic phase is harder than the ferritic phase owing to the presence of solidified carbon atoms in the crystal lattice[34] Therefore, the cooling rate of laser thermal processing is sufficient to form a hardened surface in the Phase A containing the martensitic phase.

The Phase B layer also showed elevated hardness compared to the unprocessed and Phase C layers. This gradient likely buffers the hardness mismatch at the interface between Phase A and Phase C layers, minimizing cracking. The Phase C layer exhibited hardness comparable to the unprocessed material.

Corrosion resistance.—Anodic polarization tests were performed to investigate the effect of laser thermal processing on the corrosion resistance of stainless steel. Measurements were conducted on the surface of the as-laser-thermal-processed (as-processed) specimen, and polished surfaces exposing individual phases (A, B, and C).

The surface of the as-processed specimen was thermally oxidized to a dull brown color. Figure 6 presents polarization curves of the unprocessed, 950 W-processed, and 2000 W-processed specimens. The unprocessed specimen exhibited a passive region with a low current density below 10^{-6} A cm^{-2}, followed by a sharp current increase, indicating pitting corrosion. The E_{pit} value was approximately 0.1 V, and the average E_{pit} was 0.056 ± 0.039 V, which was the lowest among all tested conditions.

As shown in Fig. 6, several transient current spikes were observed prior to the rapid current increase, indicating metastable

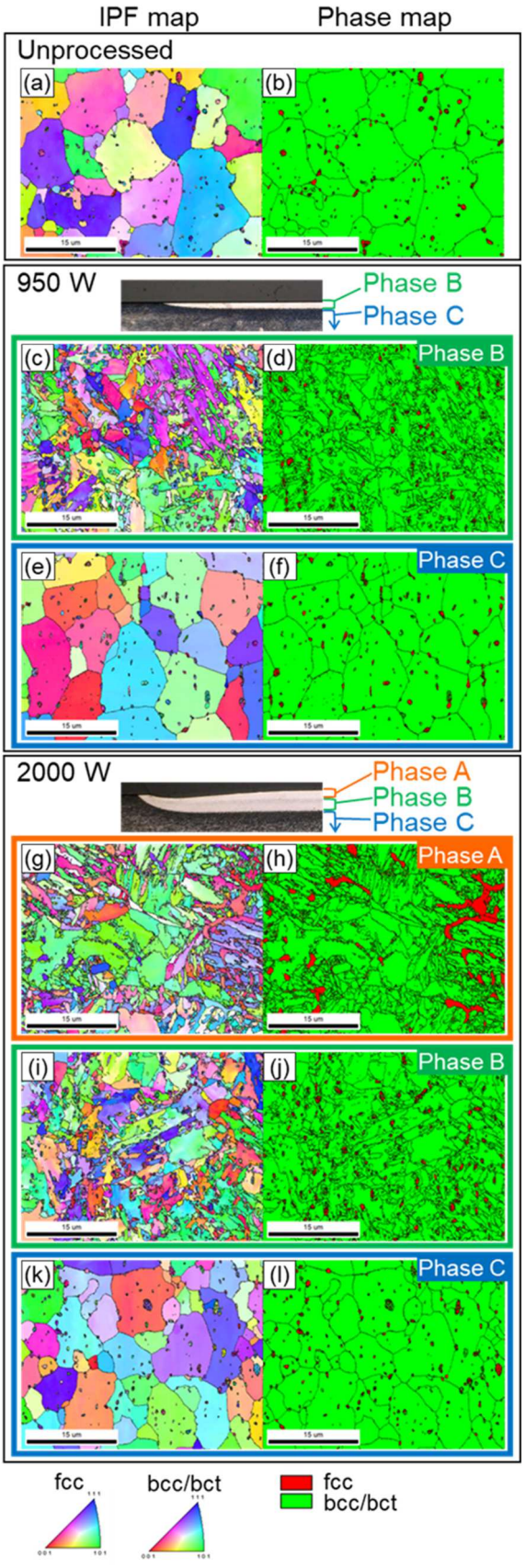

Figure 3. IPF and phase maps obtained from EBSD analysis: (a) and (b) maps of the unprocessed specimen; (c)–(f) Phase B and C maps of the specimen subjected to laser thermal processing at 950 W; (g)–(l) Phase A, B, and C maps of the specimen subjected to laser thermal processing at 2000 W.

pitting events associated with repeated pit initiation and repassivation. In contrast, small fluctuations in the low-current region are attributed to instrumental noise near the detection limit of the potentiostat and do not represent metastable pitting behavior. Notably, the frequency of metastable pitting events decreases from the unprocessed specimen to Phase B and further to Phase A, suggesting a reduction in the number of active sites for localized corrosion. This behavior is consistent with the reduction or elimination of MnS inclusions, which are known to act as preferential initiation sites for pitting corrosion.

In contrast, the as-processed specimens exhibited lower E_{corr} values than the unprocessed specimen and showed active dissolution without the formation of a stable passive region. Cross-sectional SEM observations revealed that the thermally formed oxide layer has a thickness of approximately 2–3 μm. During polarization, dissolution proceeds within this oxide layer, preventing exposure of the underlying microstructure. As a result, passive film formation is suppressed, and active dissolution persists, leading to lower corrosion resistance.

The thermally oxidized layer is relatively thick and exhibits a rough and inhomogeneous morphology, which is unfavorable for the formation of a stable passive film. Furthermore, spontaneous regeneration of a protective passive film in air is considered limited under such conditions. The time-dependent evolution of this surface layer should be investigated in future work.

The thermally oxidized layer was removed by polishing, exposing the flat surface. After polishing, specimens processed at 950 and 2000 W show improved passivation and pitting behavior, as evident in Fig. 6. The specimens processed at 2000 W exhibited a higher pitting potential than the unprocessed specimen. As shown in Fig. 3, the top surfaces of the specimens processed at 950 and 2000 W correspond to Phases B and A, respectively. The higher E_{pit} value of the 2000 W specimen compared to the 950 W specimen indicates that the Phase A layer has superior corrosion resistance to the Phase B layer. The transient peaks observed in the polarization curves are attributed to metastable pitting events, which involve repeated initiation and repassivation of localized corrosion sites. In contrast, the small fluctuations observed in the low current density region are attributed to instrumental noise near the detection limit of the potentiostat and do not represent metastable pitting behavior. The frequency and magnitude of these events depend on the microstructure and are influenced by the presence or reduction of corrosion-inducing inclusions such as MnS.

Consequently, the corrosion resistance of the newly formed layers via laser thermal processing (Phases A, B, and C) was evaluated to assess the relationship between thermal processing and the corrosion resistance of martensitic stainless steel. The inner layers of all processed specimens exhibited passive regions and subsequent pitting corrosion at higher applied potentials. The E_{pit} values of the Phase A and B layers were consistently higher than those of the unprocessed specimens. Figure 7 summarizes the E_{pit} values obtained from the anodic polarization measurements for all the specimens.

The corrosion resistances of various layers in the processed specimens subjected to laser thermal processing under identical conditions were compared. The polarization curves of the Phase A layer for specimens processed at 3500 W exhibit the highest E_{pit} value, as presented in Fig. 8. To quantitatively compare the corrosion behavior of each layer, the corrosion potential (E_{corr}), corrosion current density (i_{corr}), and E_{pit} are summarized in Table III. The i_{corr} values were determined by the Tafel extrapolation method using the linear regions of the anodic and cathodic branches. The results indicate that the Phase A layer exhibits the lowest i_{corr} and highest E_{pit}, whereas the Phase B layer shows a higher i_{corr}, suggesting more active dissolution behavior.

Each Phase A layer exhibited an evident passive region without any current spike, followed by a rapid increase in current owing to pitting corrosion at higher applied potentials. The Phase A layers

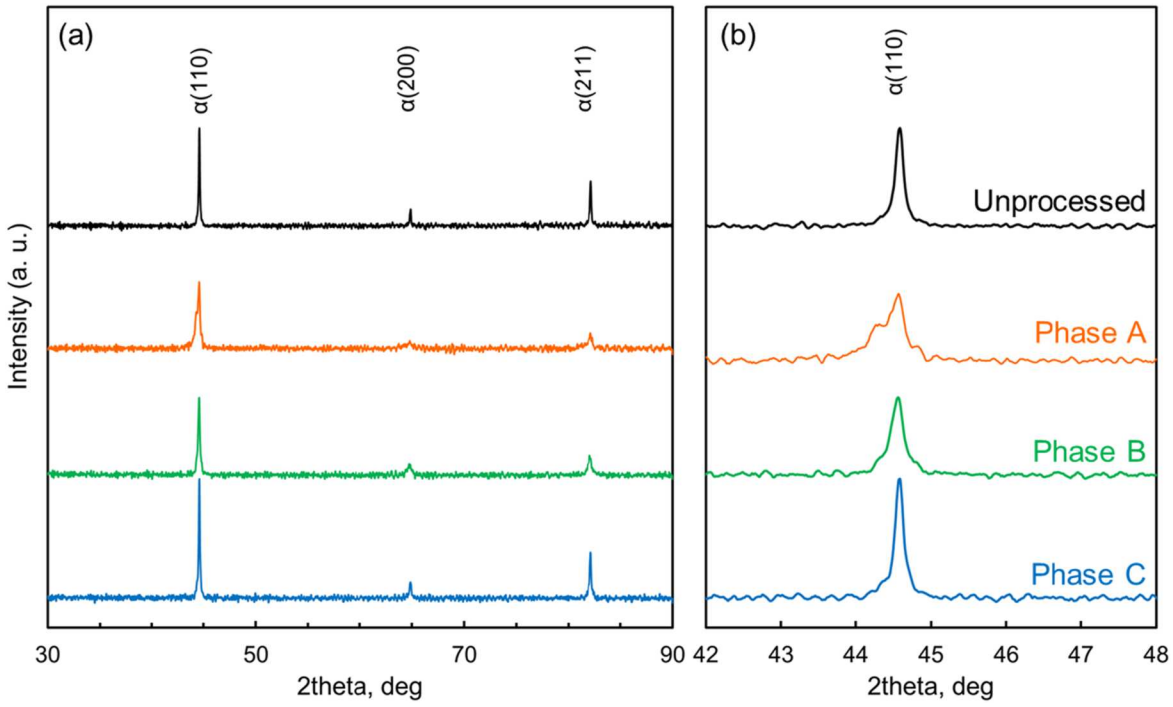

Figure 4. XRD patterns of the unprocessed specimen and the specimen subjected to laser thermal processing at 2000 W.

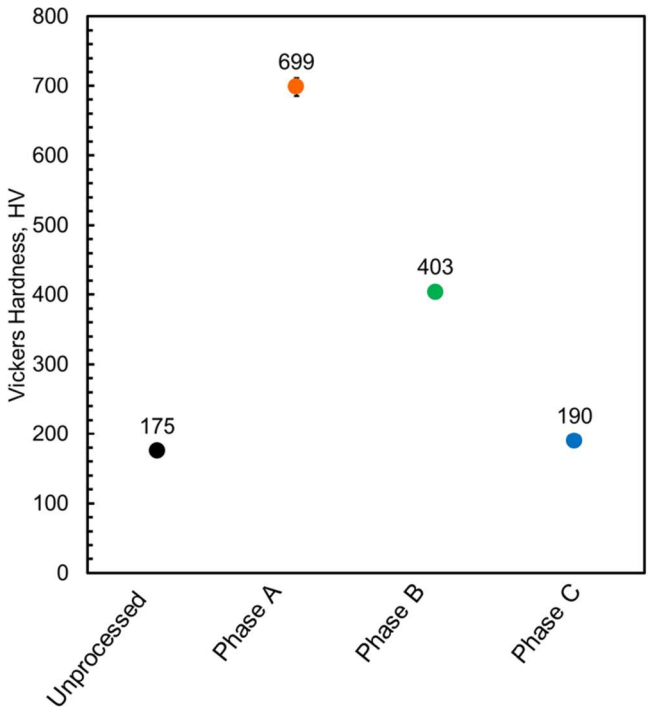

Figure 5. Vickers microhardness values of the unprocessed specimen and the specimen subjected to laser thermal processing at 2000 W.

under all processing conditions exhibited much higher E_{pit} values than those of the unprocessed specimens. In addition, the Phase A layers showed almost no indications of metastable pitting, unlike the unprocessed specimen. The Phase B layer also exhibited a passive region accompanied by a current spike, indicating metastable pitting. Subsequently, it exhibited growth-type pitting corrosion similar to the other specimens. The E_{pit} values of the Phase B layer were slightly higher than those of the unprocessed specimens. The phase C layer exhibited corrosion behavior similar to that of the unprocessed specimen; metastable pitting initiated near the E_{corr}, and growth-type pitting corrosion was observed at potentials ranging from approximately 0 to 0.1 V, comparable to the unprocessed specimen. Based on the experimental results, the corrosion resistance of the newly formed layers produced by laser thermal processing followed the order: Phase A layer > Phase B layer > Phase C layer. The thermal history of the Phase C layer, located just below the Phase B layer, showed almost no detrimental effect on corrosion resistance. This is consistent with the hardness evaluation results shown in Fig. 5.

The EBSD measurements (Fig. 3) show that the Phase A and B layers are martensitic and exhibit similar microstructures. However, their corrosion resistances are markedly different. This suggests that microstructure is not the dominant factor governing the corrosion resistance of the 420J2 stainless steel. As described in the Introduction, MnS inclusions are well known to be capable of inducing corrosion in stainless steels. Although the likelihood of MnS inclusions is low, even a single exposed MnS inclusion on the surface can trigger corrosion.

Figure 9 shows the SEM images and EDS maps of the unprocessed specimen, the Phase A layer of the specimen processed at 3500 W, and the Phase B layer of the specimen processed at 2000 W. Inclusions containing Mn and S can be observed in the unprocessed specimen, as shown in Fig. 9a. These MnS inclusions led to pitting corrosion at low potentials. In contrast, no MnS inclusions can be identified in the Phase A layer of the 3500 W processed specimen, as shown in Fig. 9b. While small MnS particles may still be present, they do not induce pitting corrosion.33 On the other hand, MnS inclusions with sizes of several micrometers are clearly observed in the Phase B layer, as shown in Fig. 9c, similar to those in the unprocessed specimen. This indicates that, unlike the remelted Phase A layer, the Phase B layer retains MnS inclusions due to the absence of melting during laser processing.

Instead, submicron-sized spherical inclusions containing Si and O were distributed across the entire surface. These inclusions are considered to originate from Si added as a deoxidizer.[35–37] The wavy surface morphology shown in Fig. 1, together with the formation of these fine inclusions, indicates that melting and subsequent rapid solidification occurred within a very short time during laser processing of the Phase A layer. Under such conditions, the original

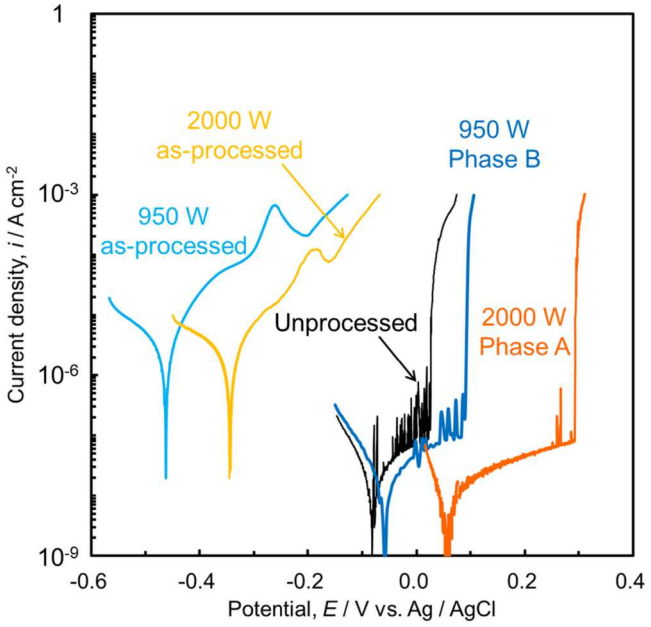

Figure 6. Polarization curves of unprocessed and laser-thermal-processed specimens.

inclusions were dissolved in the molten pool, and only a limited amount of impurities had sufficient time to reprecipitate as fine inclusions. Consequently, the formation of corrosion-inducing MnS inclusions is significantly suppressed in the Phase A layer, which contributes to its enhanced corrosion resistance. Although MnS inclusions may still exist at sizes below the detection limit of SEM, their role as dominant pit initiation sites is considered to be substantially reduced. Instead, pitting corrosion in the Phase A layer is considered to initiate at submicron-sized inclusions such as Si-based oxides or other microstructural heterogeneities. However, due to their small size and relatively homogeneous distribution, the local electrochemical heterogeneity is reduced, resulting in a lower probability of stable pit formation and thus improved corrosion resistance.

Each layer is redefined based on the observed thermal and structural changes. Phase A is remelted by laser irradiation and is therefore defined as the remelted layer. In contrast, the Phase B layer is not melted by the laser heat; instead, it undergoes a phase transformation. Therefore, Phase B is defined as the phase-transformed layer. The Phase C layers exhibit E_{pit} values similar to those of the unprocessed specimens. Additionally, the Phase C layer shows XRD spectra, microstructure, and Vickers microhardness values almost identical to those of the unprocessed specimen (Figs. 3–5). Therefore, although the Phase C layer is heated by laser irradiation, its microstructure remains unchanged and retains the same characteristics as the unprocessed material. As such, the Phase C layer can be regarded as the substrate.

The optimal laser processing conditions are discussed at the end of this section. A comparison of the results obtained under identical laser thermal processing conditions revealed that the Phase A layer exhibited significantly improved corrosion resistance. However, the E_{pit} of the Phase A layer varied under different laser power levels. On average, E_{pit} showed an increasing trend with increasing irradiation power up to 3500 W. Therefore, the Phase A layer processed at 3500 W was confirmed to exhibit the highest corrosion resistance.

The E_{pit} value of the specimen processed at 4000 W, the highest power condition in this study, was lower than that of the specimen processed at 3500 W. This reduction is attributed to the formation of cracks induced by excessive thermal stresses during rapid heating and cooling. Figure 10 shows the optical micrographs of the cross-section of the specimen processed at 4000 W. Cross-sectional observations revealed cracks penetrating from the top surface into

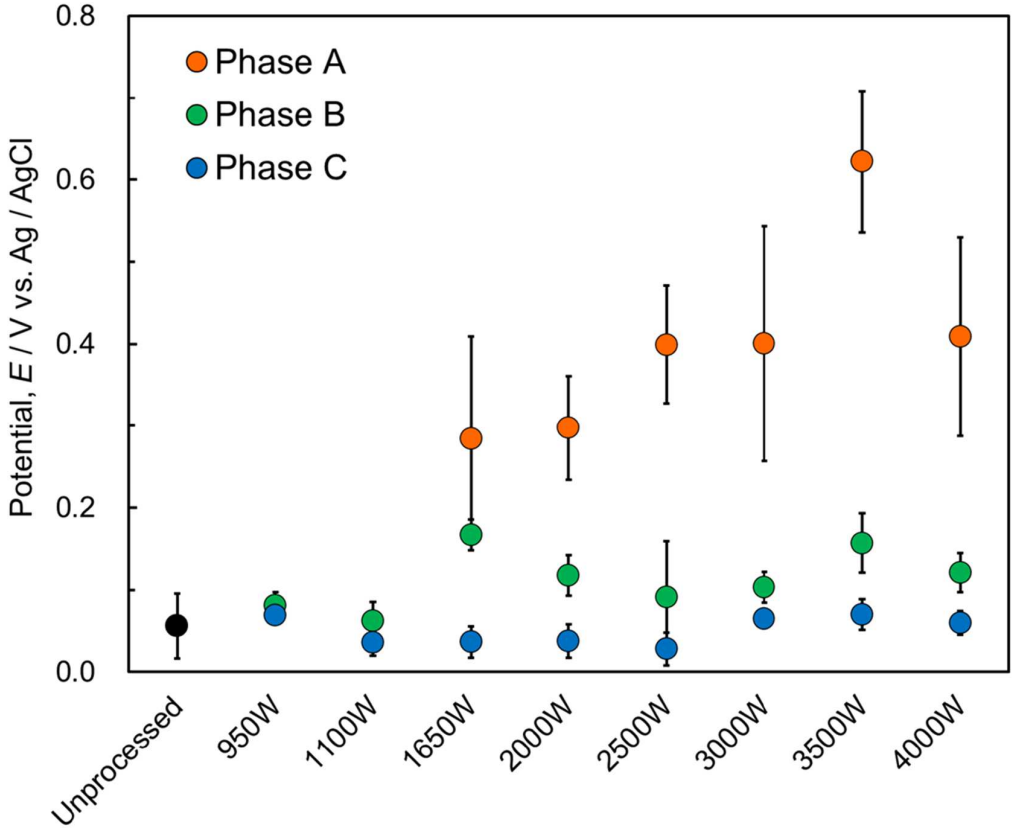

Figure 7. E_{pit} values of unprocessed and laser-thermal-processed specimens for each layer and irradiation power.

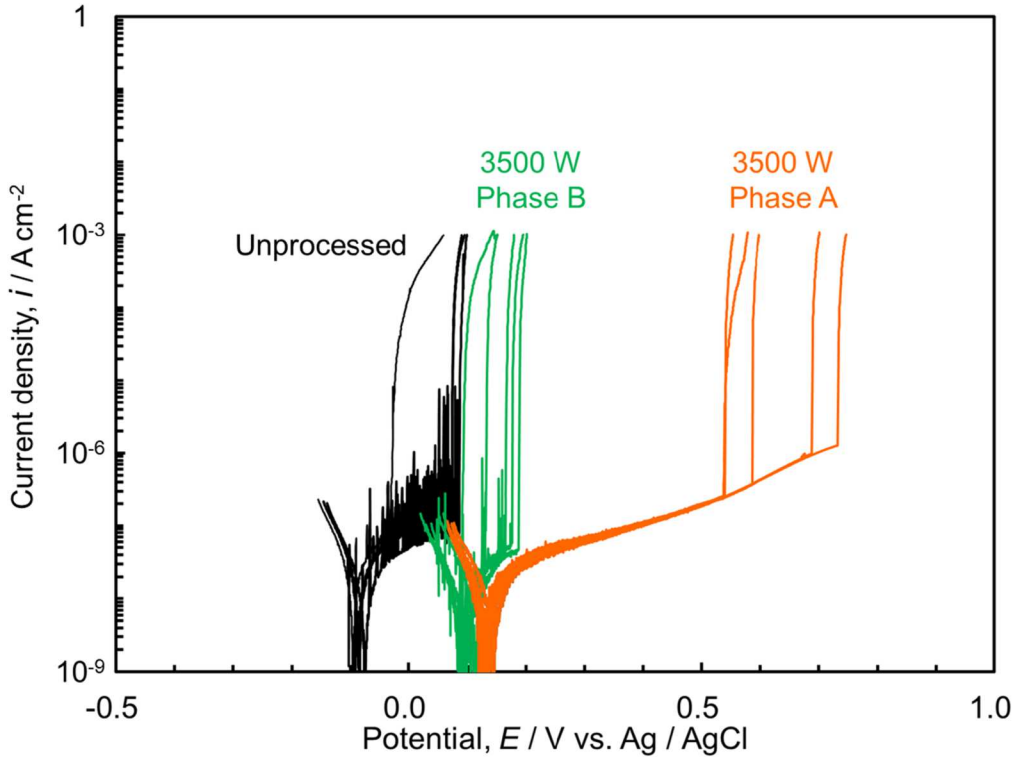

Figure 8. Polarization curves of the unprocessed specimen and the Phase A and Phase B layers processed at 3500 W.

Table III. Summary of E_{corr}, i_{corr}, and E_{pit} values for unprocessed and laser-processed specimens (mean ± standard deviation).

	E_{corr} (V)	i_{corr} (A cm^{-2})	E_{pit} (V)
Unprocessed	−0.084 ± 0.0079	(7.8 ± 0.85) × 10^{-9}	0.11 ± 0.060
Phase A (3500 W)	−0.13 ± 0.0056	(7.8 ± 3.0) × 10^{-10}	0.62 ± 0.086
Phase B (3500 W)	−0.094 ± 0.015	(1.8 ± 0.46) × 10^{-8}	0.16 ± 0.036

Table IV. Microstructure, Vickers hardness, corrosion-inducing inclusions, and corrosion resistance of the layer formed by laser thermal processing.

	Phase	Vickers hardness (HV)	MnS inclusions	Corrosion resistance
Phase A: Remelted	Martensite+Austenite	699	Absence	High
Phase B: Phase transformed	Martensite+Austenite	403	Presence	Moderate
Phase C: Substrate	Ferrite+Residual austenite	190	Presence	Low
Untreated	Ferrite+Residual austenite	175	Presence	Low

the inner layers in both the 3500 and 4000 W specimens (before grinding), likely due to excessive residual stresses induced by rapid cooling. The cracks in the specimens processed at 4000 W were deeper than those in the specimens processed at 3500 W. Although cracks were not confirmed to act directly as initiation sites, they can form geometrical features similar to micro-pits. Such features may locally restrict solution transport and promote the formation of occluded environments, thereby facilitating localized corrosion. In contrast, the cracks in the 3500 W specimen were completely removed after grinding to expose the intact Phase A layer. Therefore, the specimen processed at 3500 W exhibited the highest E_{pit} among all the specimens examined in this study.

The effects of laser irradiation on corrosion resistance can be summarized as follows: higher laser irradiation output tends to improve corrosion resistance to some extent. However, excessive power can introduce cracks, which hinder the localized corrosion resistance of martensitic stainless steel. Therefore, an optimal combination of irradiation power (3000–3500 W in this study) and grinding depth is crucial for achieving maximum corrosion resistance through laser thermal processing.

This discussion can be further summarized as follows: when the specimens were irradiated with laser power below 1100 W, no remelting zone was formed, resulting in moderate heating and quenching. Consequently, a Phase B (phase-transformed) layer was formed on the surface via laser thermal processing. Alternatively, when the laser power exceeded 1650 W, a remelted layer was newly formed on the surface. The Phase A (remelted) layer and the underlying Phase B (phase transformed) layer were formed on the surface of the specimens through laser thermal processing. The relationship between the mechanical properties and corrosion

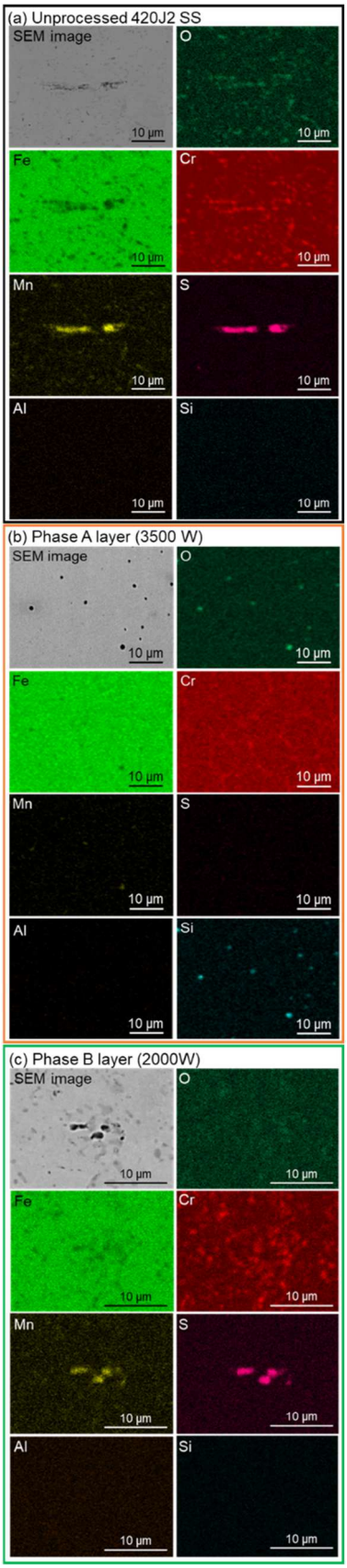

Figure 9. SEM images and EDS mapping images of (a) the unprocessed specimen, (b) the Phase A layer processed at 3500 W, and (c) the Phase B layer processed at 2000 W. MnS inclusions are clearly observed in the unprocessed specimen and the Phase B layer, whereas they are not detected in the Phase A layer.

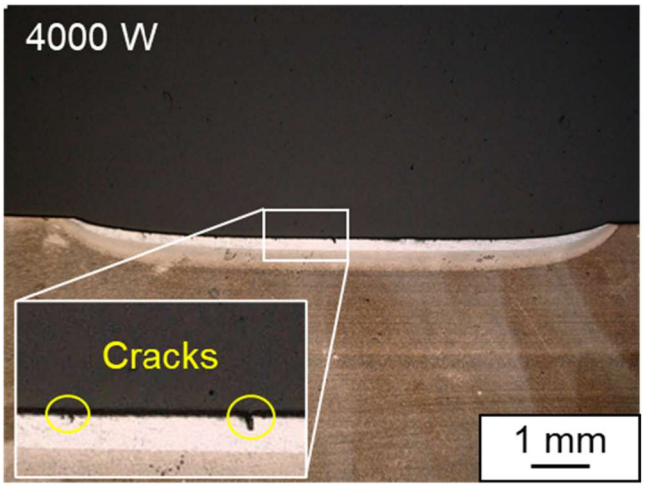

Figure 10. Optical micrographs of the cross-section of the specimen after laser thermal processing at 4000 W.

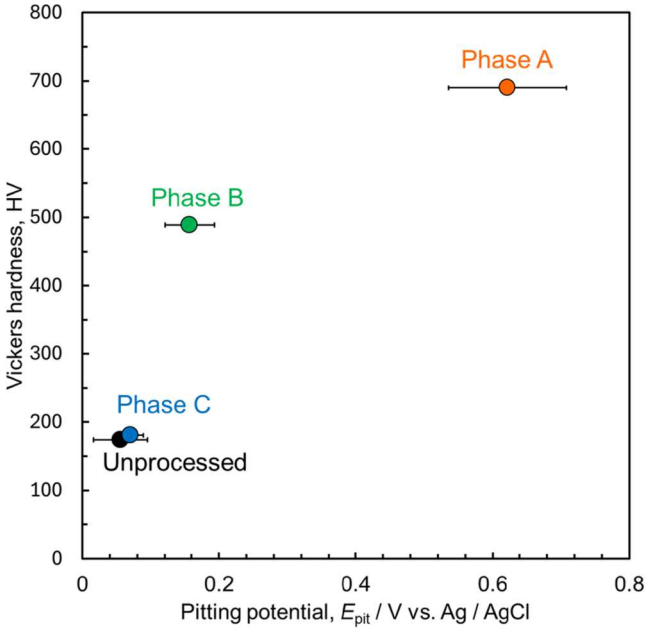

Figure 11. Pitting corrosion potential and Vickers hardness of unprocessed and laser thermal processed specimen at 2000 W. The Phase A layer of the laser-thermal-processed specimen exhibits both high corrosion resistance and high hardness.

resistance achieved via laser thermal processing is presented in Fig. 11 and Table IV. Laser thermal processing produced a remelted (Phase A) layer with reduced formation of corrosion-inducing inclusions and enhanced martensitization. Typically, in stainless steel, hardness and corrosion resistance are inversely related. However, in the remelted (Phase A) layer, both high hardness and high corrosion resistance were simultaneously achieved.

This study demonstrated that laser thermal processing can effectively enhance both hardness and corrosion resistance. However, certain limitations exist. Martensitic stainless steel hardened by quenching must typically undergo additional heat treatment (tempering) before practical application. Tempering is essential to mitigate brittleness while maintaining adequate hardness. Therefore, further studies are needed to investigate the effects of tempering treatment at 423–473 K on the corrosion resistance of laser-thermal-processed martensitic stainless steels.

Conclusion

In this study, we investigated whether the high corrosion resistance of 420J2 stainless steel—attributed to the formation of microstructures with reduced MnS inclusions, as observed in LPBF—can be achieved solely through laser irradiation. The following conclusions were drawn:

1. Different microstructural layers were formed after laser thermal processing, including a remelted layer and a phase-transformed layer.
2. Both the remelted and phase-transformed layers were martensitic and exhibited high hardness.
3. The remelted and phase-transformed layers also demonstrated improved corrosion resistance compared to the unprocessed specimen, with the remelted layer showing significantly better corrosion resistance.
4. Higher laser irradiation power resulted in a deeper remelted layer. However, excessive laser power led to the formation of surface cracks, which adversely affected corrosion resistance.
5. In the remelted layer, the formation of corrosion-inducing inclusions (such as MnS) was suppressed due to the rapid remelting and solidification induced by laser irradiation. Consequently, laser-thermal-processed stainless steel exhibited enhanced corrosion resistance.

Therefore, laser thermal processing is a promising technique for achieving both high corrosion resistance and hardness, an outcome that is typically difficult to attain using conventional methods for martensitic stainless steels.

Acknowledgments

This study was supported by JSPS KAKENHI (grant number: JP22KJ1204, JP23K19179, JP24K17529, JP24K01223, JP26K17673). This study was also supported by The Japan Institute of Metals and Materials (JIMM) grants-in-aid for frontier research. This study was supported by Institute of Light Metals (ILM) Joint Usage/Research Grant, Kumamoto University & University of Toyama. This work was supported by the Division of Instrumental Analysis at University of Toyama.

ORCID

Tomoyo Manaka https://orcid.org/0000-0001-9649-2035
Yusuke Tsutsumi https://orcid.org/0000-0002-9483-1256
Mitsuhiro Goto https://orcid.org/0009-0000-2426-3233
Mariko Kadowaki https://orcid.org/0000-0002-8988-3545
Yoshiharu Murase https://orcid.org/0000-0001-7390-851X
Hideki Katayama https://orcid.org/0000-0001-7947-4687
Takuya Ishimoto https://orcid.org/0000-0003-0081-0591
Takao Hanawa https://orcid.org/0000-0003-1688-1749

References

1. J. Pan, *Front. Mater.*, **7**, 133 (2020).
2. C. O. A. Olsson and D. Landolt, *Electrochimic. Acta*, **48**, 1093 (2003).
3. E. Hamada, K. Yamada, M. Nagoshi, N. Makiishi, K. Sato, T. Ishii, K. Fukuda, S. Ishikawa, and T. Ujiro, *Corros. Sci.*, **52**, 3851 (2010).
4. L. Gardner, *Prog. Struct. Eng. and Mater.*, **7**, 45 (2005).
5. L. D. Barlow and M. Du Toit, *J. Mater. Eng. Perform.*, **21**, 1327 (2012).
6. A. Chiba, I. Muto, Y. Sugawara, and N. Hara, *J. Electrochem. Soc.*, **160**, C511 (2013).
7. A. Chiba, I. Muto, Y. Sugawara, and N. Hara, *J. Electrochem. Soc.*, **159**, C341 (2012).
8. D. Li, F. Huang, X. Lei, and Y. Jin, *Corros. Sci.*, **211**, 110860 (2023).
9. R. Ke and R. Alkire, *J. Electrochem. Soc.*, **139**, 1573 (1992).
10. G. S. Frankel, *J. Electrochem. Soc.*, **145**, 2186 (1998).
11. M. P. Ryan, D. E. Williams, R. J. Chater, B. M. Hutton, and D. S. McPhail, *Nature*, **415**, 770 (2002).
12. J. H. Park and Y. Kang, *Steel Res. Int.*, **88**, 1700130 (2017).
13. H. L. Jia, H. Sun, H. Z. Wang, Y. Wu, and H. W. Wang, *Int. J. Adv. Manuf. Technol.*, **113**, 2413 (2021).
14. Y. Tsutsumi, T. Ishimoto, T. Oishi, T. Manaka, P. Chen, M. Ashida, K. Doi, H. Katayama, T. Hanawa, and T. Nakano, *Addit. Manuf.*, **45**, 102066 (2021).
15. S. H. Sun, T. Ishimoto, K. Hagihara, Y. Tsutsumi, T. Hanawa, and T. Nakano, *Scr. Mater.*, **159**, 89 (2019).
16. Y. Zhao, H. Xiong, X. Li, W. Qi, J. Wang, Y. Hua, T. Zhang, and F. Wang, *Corros. Commun.*, **2**, 55 (2021).
17. Q. Chao, V. Cruz, S. Thomas, N. Birbilis, P. Collins, A. Taylor, P. D. Hodgson, and D. Fabijanic, *Scr. Mater.*, **141**, 94 (2017).
18. M. Kazemipour, M. Mohammadi, E. Mfoumou, and A. M. Nasiri, *JOM*, **71**, 3230 (2019).
19. G. Sander, S. Thomas, V. Cruz, M. Jurg, N. Birbilis, X. Gao, M. Brameld, and C. R. Hutchinson, *J. Electrochem. Soc.*, **164**, C250 (2017).
20. K. Saeidi, D. L. Zapata, F. Lofaj, L. Kvetkova, J. Olsen, Z. J. Shen, and F. Akhtar, *Addit. Manuf.*, **29**, 100803 (2019).
21. P. H. Chong, Z. Liu, P. Skeldon, and P. Crouse, *Appl. Surf. Sci.*, **247**, 362 (2005).
22. P. H. Chong, Z. Liu, X. Y. Wang, and P. Skeldon, *Thin Solid Films*, **453**, 388 (2004).
23. Y. Tsutsumi, M. Shimabukuro, T. Manaka, M. Goto, M. Kadowaki, T. Hashimoto, M. Kawashita, T. Ishimoto, and H. Katayama, *APL Mater.*, **14**, 051105 (2026).
24. A. Conde, I. Garcia, and J. J. de Damborenea, *Corros. Sci.*, **43**, 817 (2001).
25. T. N. Le and Y. L. Lo, *Mater. Des.*, **179**, 107866 (2019).
26. B. Song, T. Yu, X. Jiang, W. Xi, and X. Lin, *Int. J. Mech. Sci.*, **165**, 105207 (2020).
27. Y. Tomota, H. Tokuda, S. Torii, and T. Kamiyama, *Mater. Sci. Eng. A*, **434**, 82 (2006).
28. T. W. Liu, D. H. Ping, T. Ohmura, and M. Ohnuma, *J. Mater. Sci.*, **53**, 2976 (2018).
29. E. P. Yelsukov, E. V. Voronina, and V. A. Barinov, *J. Magn. Magn. Mater.*, **115**, 271 (1992).
30. K. Sumiyama, Y. Hirose, and Y. Nakamura, *J. Phys. Soc. Jpn.*, **59**, 2963 (1990).
31. Y. Lu, H. X. Yu, and R. D. Sisson, *Mater. Sci. Eng. A*, **700**, 592 (2017).
32. P. Landgraf, J. Man, M. Cieslar, and J. Dlouhy, *Metals*, **11**, 1071 (2021).
33. W. Jiang, Y. Liu, X. Zhang, and H. Wang, *Metals*, **14**, 322 (2024).
34. B. Hutchinson, J. Hagstrom, O. Karlsson, D. Lindell, M. Tornberg, F. Lindberg, and M. Thuvander, *Acta Mater.*, **59**, 5845 (2011).
35. Z. Zhan, G. Wang, R. Shi, W. Zhang, Y. Zhang, and G. Cheng, *ISIJ Int.*, **63**, 622 (2023).
36. K. Suzuki, S. Ban-ya, and M. Hino, *ISIJ Int.*, **42**, 146 (2002).
37. L. Su, X. Li, Y. Zhang, Z. Zhang, and J. Li, *J. Mater. Res. Technol.*, **15**, 1949 (2021).